Reproducibility of Measuring Lamina Cribrosa Pore Geometry in Human and Nonhuman Primates with In Vivo Adaptive Optics Imaging

Kevin M. Ivers, Chaohong Li, Nimesh Patel, Nripun Sredar, Xunda Luo, Hope Queener, Ronald S. Harwerth, and Jason Porter

Purpose. The ability to consistently resolve lamina cribrosa pores in vivo has applications in the study of optic nerve head and retinal disease mechanisms. Repeatability was assessed in imaging laminar pores in normal living eyes with a confocal adaptive optics scanning laser ophthalmoscope (AOSLO).

Methods. Reflectance images (840 nm) of the anterior lamina cribrosa were acquired using the AOSLO in four or more different sessions in two normal rhesus monkey eyes and three normal human eyes. Laminar pore areas, elongations (ratio of major to minor axes of the best-fit ellipse) and nearest neighbor distances were calculated for each session. Measurement repeatability was assessed across sessions.

Results. Pore areas ranged from 90 to 4365 μm^2 in monkeys and 154 to 6637 μm^2 in humans. Mean variabilities in measuring pore area and elongation (i.e., mean of the standard deviation of measurements made across sessions for the same pores) were 50 μm^2 (6.1%) and 0.13 (6.7%), respectively, in monkeys and 113 μm^2 (8.3%) and 0.17 (7.7%), respectively, in humans. Mean variabilities in measuring nearest neighbor distances were 1.93 μm (5.2%) in monkeys and 2.79 μm (4.1%) in humans. There were no statistically significant differences in any pore parameters across sessions (ANOVA, $P > 0.05$).

Conclusions. The anterior lamina cribrosa was consistently imaged in vivo in normal monkey and human eyes. The small intersession variability in normal pore geometry suggests that AOSLO imaging could be used to measure and track changes in laminar pores in vivo during glaucomatous progression. (*Invest Ophthalmol Vis Sci.* 2011;52:5473–5480) DOI:10.1167/iovs.11-7347

Glaucoma is a multifaceted group of eye diseases that results in the degeneration of retinal ganglion cell axons and the death of retinal ganglion cells (RGCs). The mechanisms of glaucomatous damage (e.g., mechanical, vascular, and glial) are not fully understood. Although several of these factors likely contribute to RGC death, substantial evidence suggests that the initial site of axonal injury likely occurs at the level of the lamina cribrosa in the optic nerve head (ONH).[1–11] In humans and nonhuman primates, the lamina cribrosa is a three-dimensional porous structure consisting of flexible beams of collagenous tissue that support and nourish the RGC axons passing through it from the retina to the brain.[12] Increases in intraocular pressure (IOP) impart stress and strain on the lamina,[13–15] resulting in a posterior bowing and stretching of the load-bearing laminar beams[12,16] and potential increases in laminar pore area and elongation (or more elliptically shaped pores). Stretching and deformation of the laminar beams (and associated pores) could sheer or damage encompassed axons and laminar capillaries, thereby hampering axonal transport, blood flow and the diffusion of nutrients,[17] and/or the neurotrophic support provided to the axons by alterations in glial cells.[18]

ONH tissues have been examined in human glaucomatous eyes and nonhuman primate models of experimental glaucoma. Postmortem histologic studies have shown significant changes in prelaminar and laminar tissues within the ONH in early experimental glaucoma.[16,19,20] Additional ex vivo studies in glaucomatous human and nonhuman primate eyes have described early changes in laminar morphology and position,[16,21] laminar pore geometry,[22] and the composition and architecture of laminar connective tissues.[20,23] In light of this work, there is a growing consensus that in vivo studies are necessary to validate ex vivo results and examine longitudinal changes during glaucoma.[24,25]

The lamina cribrosa has been examined in vivo. Fontana et al.[26] imaged anterior laminar pores in living human glaucomatous eyes using a modified confocal scanning laser ophthalmoscope (SLO) and showed that pore area and elongation were larger in eyes with more severe glaucoma. However, images were taken using a wide field of view (20°) and were not of high resolution because of the presence of ocular aberrations. Therefore, the size and total number of pores that could be resolved and the number of subjects in which laminar pores could be successfully imaged were limited. Vilupuru et al.[27] used a confocal adaptive optics scanning laser ophthalmoscope (AOSLO), an instrument that noninvasively provides cellular-level images through a correction of the eye's aberrations, to improve the resolution and contrast of laminar images in vivo in nonhuman primates with experimental glaucoma. This study quantified laminar pore geometries in three diseased monkey eyes, each at a single time point. However, changes in pore geometry with disease were not investigated. Recent studies have combined adaptive optics with optical coherence tomography (OCT) to image the human lamina cribrosa in three spatial dimensions,[28,29] but a quantitative analysis of laminar geometry and pore structure has not been reported.

From the College of Optometry, University of Houston, Houston, Texas.

Supported by National Institutes of Health (NIH) Grants P30 EY07551 and R01 EY01139; the Texas Advanced Research Program under Grant G096152; and the University of Houston College of Optometry. The software used for the adaptive optics system in this research was partially developed by Alfredo Dubra-Suarez, funded by a Career Award from the Burroughs Wellcome Fund, and Kamran Ahmad, funded by NIH grant BRP-EY01437 and the National Science Foundation Science and Technology Center for Adaptive Optics.

Submitted for publication February 8, 2011; revised April 8, 2011; accepted April 21, 2011.

Disclosure: **K.M. Ivers**, None; **C. Li**, None; **N. Patel**, None; **N. Sredar**, None; **X. Luo**, None; **H. Queener**, None; **R.S. Harwerth**, None; **J. Porter**, None

Corresponding author: Kevin M. Ivers, College of Optometry, University of Houston, 505 J. Davis Armistad Building, Houston, TX 77204; kmivers@uh.edu.

We have assessed the repeatability of imaging and quantifying laminar pores in vivo in two normal macaque and three normal human eyes using an AOSLO at different time points. Statistical tests were performed to investigate whether significant differences were present in any analyzed laminar pore parameters within and across imaging sessions. This study provides an important first step in understanding the feasibility of using in vivo AOSLO imaging to assess laminar structure in normal eyes, human glaucomatous eyes, and nonhuman primate eyes with experimentally induced glaucoma.

METHODS

All animal care experimental procedures were approved by the University of Houston's Institutional Animal Care and Use Committee and adhered to the ARVO Statement for the Use of Animals in Ophthalmic and Vision Research. All research in human subjects adhered to the tenets of the Declaration of Helsinki, and the study protocol was approved by the University of Houston's Committee for the Protection of Human Subjects. Informed consent was obtained for each human subject.

The anterior lamina cribrosa was examined in vivo in two normal rhesus monkeys (*Macaca mulatta*), aged 1.5 (M036) and 7 (M057) years, and three normal humans: a 24-year-old woman of Indian descent (H058), a 31-year-old man of Indian descent (H030), and a 47-year-old Caucasian man (H055). All human eyes had ≤ -1.50 D of spherical refractive error and ≤ -1.00 D of cylinder. The monkeys were anesthetized with 20 to 25 mg/kg ketamine, 0.8 to 0.9 mg/kg xylazine, and 0.04 mg/kg atropine sulfate to minimize eye movements during in vivo imaging.[30] Monkeys and humans were dilated with 2.5% phenylephrine and 1% tropicamide. A speculum was used to hold the monkey's eyelid open, and a contact lens was placed on the monkey eye to prevent corneal dehydration during imaging.

Fundus Imaging

Before AOSLO imaging, monkey and human eyes were imaged (Spectralis HRA+OCT; Heidelberg Engineering, Heidelberg, Germany) to acquire wide-field SLO fundus images of the ONH. The wide-field images (15°, 20°, or 30° in extent) were useful during AOSLO imaging sessions for navigating throughout the retina as the AOSLO imaging field was small (1.5°). Landmarks in the fundus images, such as vasculature, were easy to recognize and relocate across separate imaging sessions.

Biometric Measurements and Image Scaling

Axial length, anterior chamber depth and anterior corneal curvature were measured in all human and monkey eyes with an ocular biometer (IOLMaster; Carl Zeiss Meditec, AG, Jena, Germany). These biometric measurements were incorporated into a model eye to convert visual angle (in degrees) to retinal size (in micrometers). For monkeys, we generated a three-surface model eye that incorporated the biometric measurements and previously published measurements of lens thickness and curvatures corresponding to each monkey's age.[31] For humans, the biometric measurements were incorporated into a four-surface model eye as described by Li et al.[32] In both models, the location of the secondary nodal point (N') was calculated and retinal size (x) was determined with the equation:

$$\tan\theta = \frac{x}{N'R} \quad (1)$$

where θ is the visual angle and $N'R$ is the distance from N' to the retina.

AOSLO Imaging

The monkey's head was stabilized for imaging using a head mount attached to an *XYZ* translation stage. The tip, tilt, and rotation capabilities of the head mount allowed the head to be positioned for imaging the optic disc and lamina cribrosa. The translation stage was used to center the eye's pupil on the AOSLO system. Human eyes were stabilized and positioned using a custom-made bite bar attached to an *XYZ* translation stage. Subjects fixated on a laser pointer projected onto a fixation target. The pointer was moved until the ONH could be visualized in each subject.

An 840-nm superluminescent diode (Superlum, Carrigtwohill, Ireland) was used for wavefront sensing and reflectance imaging. The power of this source at the corneal plane was ~300 μW (which is greater than 10 times below the maximum permissible exposure dictated by the ANSI standards for a 1.5° field size, 1.5-hour exposure, and wavelength of 840 nm).[33,34] Aberrations were measured and corrected (10 Hz) over a dilated pupil (typically ~8 mm) using a Shack-Hartmann wavefront sensor and two deformable mirrors (or a woofer–tweeter system).[35] A high-stroke deformable mirror (Mirao 52-e; Imagine Eyes, Inc., Orsay, France) corrected large amplitude, lower order aberrations, while a lower-stroke deformable mirror (Multi-DM MEMS; Boston Micromachines, Inc., Cambridge, MA) corrected low amplitude, higher-order aberrations.

After adaptive optics correction, retinal videos were captured over a 1.5° field at a rate of 25 Hz. Through-focus images were acquired at different depths in the ONH to determine the plane of best-focus of the anterior laminar surface (Fig. 1). The plane of best-focus corresponded to the location where the edges of the anterior laminar pores first became sharpest and image brightness and contrast were optimal (Fig. 1e). When focused above the anterior surface of the lamina, the vasculature was in focus (Figs. 1a, 1b). When focused below the anterior surface, image brightness, contrast, and resolution decreased (Figs. 1k, 1l), likely due to increased light scatter and optical defocus. It was not possible to visualize the entire anterior laminar surface, as some regions were obstructed by overlying vasculature. Therefore, we imaged as much of the lamina as possible in each session. A maximum of 30 minutes was typically required to image the lamina cribrosa in a given eye. Monkeys and humans were imaged on at least four different occasions, each separated by a minimum of 1 week.

Image Processing and Analysis

AOSLO videos were processed off-line with a customized program (written in MATLAB; The MathWorks, Inc., Natick, MA) to remove image distortions caused by eye movements that occurred during video acquisition. Individual frames were first registered using a normalized cross-correlation technique. Several frames were then averaged to yield a single, high signal-to-noise registered image (Fig. 2). Montages of the lamina cribrosa were generated from the individual registered images (Photoshop; Adobe Systems, San Jose, CA).

For each montage of the anterior lamina cribrosa, individual laminar pores were identified, and four pore parameters (previously used to assess pore geometry) were calculated: pore area, elongation (ratio of major to minor axes of an ellipse best fit to each pore), centroid location, and nearest neighbor distance.[26,27] Each pore was identified manually by drawing a polygon about its edge, or boundary (Photoshop; Adobe Systems). For cases in which it was challenging to determine (from the registered image) whether a large pore actually consisted of smaller pores, through-focus videos were used to examine laminar beam orientation about the plane of best focus and make a decision. For example, pores marked with an asterisk in Figure 2c represent pores that were deemed to be a single pore (rather than a collection of smaller pores), after watching the videos. Once the pores were demarcated, the image was binarized such that the laminar pores were filled with white and the image background was black. The resultant image was imported into ImageJ (developed by Wayne Rasband, National Institutes of Health, Bethesda, MD; available at http://rsb.info.nih.gov/ij/index.html) where the area, centroid location, and major and minor axes of the best-fitted ellipse were quantified for each pore. Pore elongation was calculated by taking the ratio of the major to minor axes of the best-fitted ellipse. The nearest neighbor distance

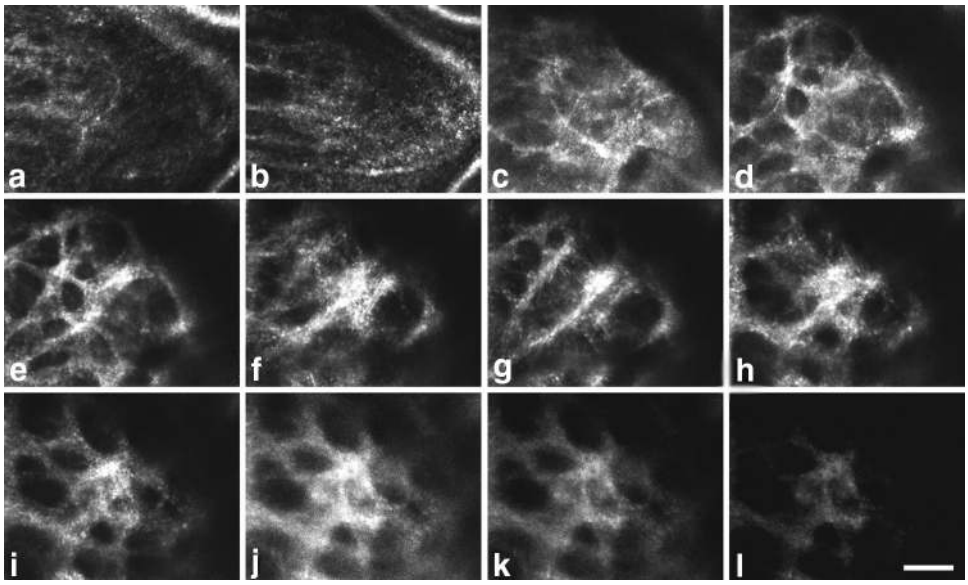

FIGURE 1. (**a**–**l**) Through-focus images of the macaque (M036) lamina cribrosa shown in an (**a**) anterior to (**l**) posterior direction. Vasculature was in focus in the most anterior sections. As the focal plane was moved posteriorly, the lamina gradually came into and went out of focus. The anterior laminar surface was judged to be in best focus when pore edges first became sharpest and image brightness and contrast were optimal (**e**). Scale bar, 50 μm.

(NND) of each pore was calculated as the minimum Euclidean distance between the centroid position of a given pore and that of its immediately surrounding neighbors.

This pore identification and quantification method was applied to montages of the anterior lamina cribrosa acquired in each imaging session. Two independent observers analyzed the same laminar pores in a single montage from a randomly selected time point in each human and monkey eye to assess the interobserver reproducibility of our pore identification and measurement method. Intraclass correlation coefficients (ICCs) accounting for two-way random effects for single measures, ICC(2,1), were calculated for each analyzed pore parameter. Pore parameters were also compared within the same eyes across imaging sessions. For each pore, the standard deviation of the mean value of each parameter across sessions was calculated to determine the variability in our imaging and measurement technique. Analysis of variance (ANOVA) tests for repeated measures were performed to compare pore parameters in each eye across all sessions. Only pores that could be imaged and quantified in all imaging sessions for each eye were included in the ANOVA. To assess our intrasession variability, our identification and quantification process was repeated three separate times on the same montage acquired in a single imaging session. Pores were identified in a random sequence in each analysis and pore parameters were calculated and compared across analyses.

RESULTS

Adaptive optics significantly improved the image quality of the lamina cribrosa in vivo in humans and macaques. Figure 3 compares SLO fundus images (Spectralis; Heidelberg Engineering) of a monkey (M057) and human (H055) ONH when best focused at the level of the lamina cribrosa (Figs. 3a, 3c) with an overlaid AOSLO montage of the anterior lamina cribrosa acquired in the same eyes (Figs. 3b, 3d). Even when best-focused at the level of the lamina, it is not possible to unambiguously resolve and quantify the majority of laminar pores using a high-quality, conventional SLO (Figs. 3a, 3c). After a correction of the eye's aberrations, AOSLO imaging provides increased resolution and contrast of the pores (Figs. 3b, 3d), particularly along their boundaries, allowing for their identification and quantification.

Figure 4 shows montages of the anterior lamina cribrosa acquired in two normal monkey eyes and three normal human eyes. Laminar pores were identified in these montages and mean pore area, elongation, and NND were calculated for each individual eye and across species. The ICCs for laminar pore area, elongation, and NND in monkey eyes were 0.87, 0.83, and 0.97, respectively. The ICCs for pore area, elongation and NND in human eyes were 0.83, 0.81, and 0.96, respectively.

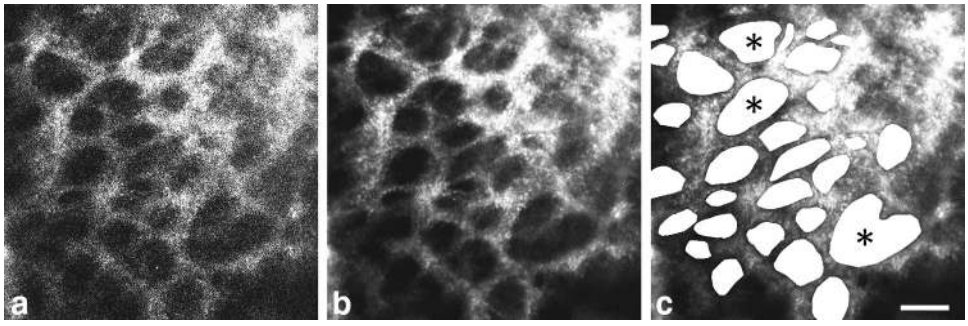

FIGURE 2. (**a**) Single frame from an AOSLO video of a macaque (M057) lamina cribrosa. Although the laminar pores can be seen, their edges are poorly defined. (**b**) Registering and averaging several frames (30 frames in this example) increased the signal-to-noise ratio. Edges and contrast of pores were greatly improved. (**c**) Individual pores were identified throughout the lamina, and pore parameters were calculated. (✱) Pores that were deemed to be a single pore (rather than a collection of smaller pores) after examining the through-focus videos. Scale bar, 50 μm.

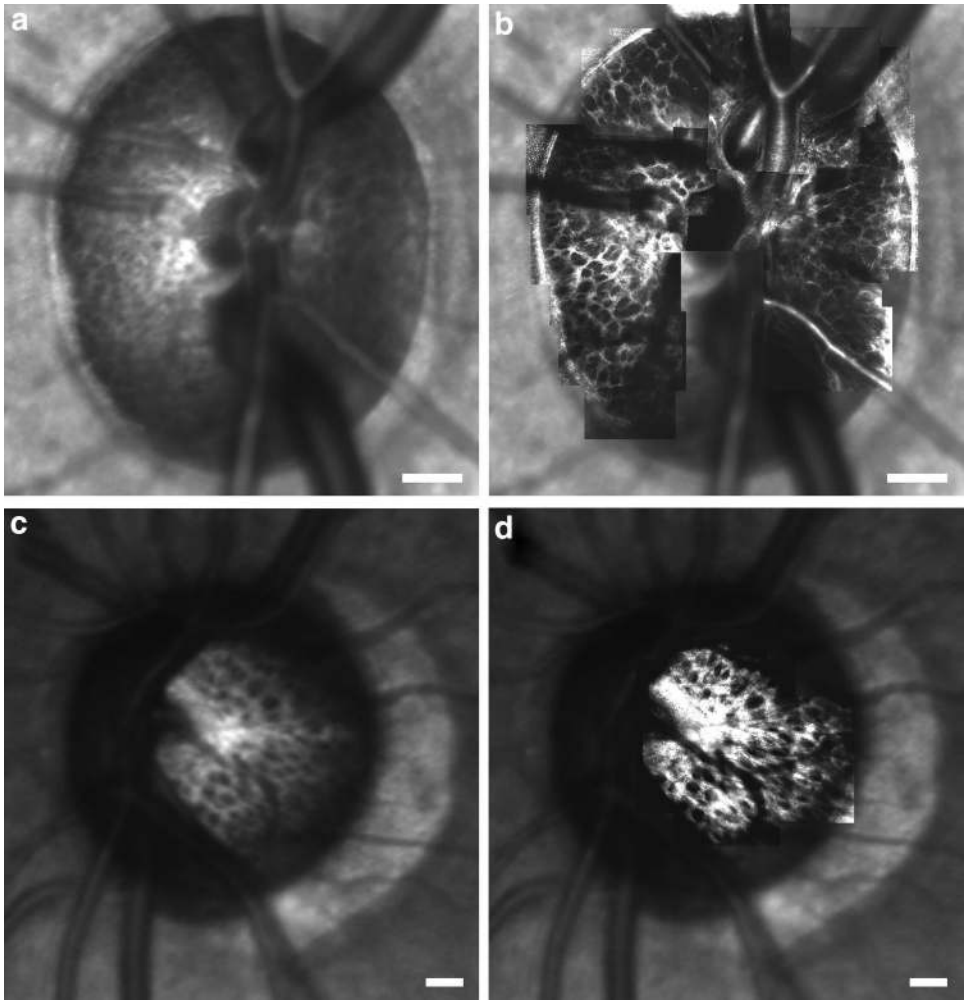

FIGURE 3. SLO images of a (**a**) primate ONH (M057) and (**c**) human ONH (H055) when best-focused on the lamina. (**b**, **d**) Same SLO images, but with the corresponding AOSLO montage overlaid on top. Resolution and contrast are improved after AO correction. Scale bar, 200 μm.

Given this excellent agreement between observers and the length of time typically required to generate a montage, subjectively delineate pore boundaries and quantify pore geometry, a single investigator examined pores at all time points in each eye.

Pore geometry results in monkeys and humans are summarized in Table 1. Sixty-eight and 87 anterior laminar pores were analyzed in monkey eyes M036 and M057, respectively, whereas 18, 23, and 53 pores were analyzed in human eyes H058, H030, and H055, respectively. On average, mean pore parameters were larger in our human subjects compared to macaques. The mean pore areas ($\pm$1 standard deviation) in macaques and humans were 973 $\pm$ 794 and 1713 $\pm$ 1414 μm^2, respectively. In macaques, pore areas ranged from 90 to 4365 μm^2, whereas pore areas ranged from 154 to 6637 μm^2 in humans. Mean elongations ($\pm$ 1 standard deviation) were 1.77 $\pm$ 0.66 and 2.00 $\pm$ 0.75 in macaques and humans, respectively, whereas mean NND ($\pm$1 standard deviation) was 36.9 $\pm$ 7.19 μm in monkeys and 69.1 $\pm$ 19.8 μm in humans.

Anterior laminar pore geometry was compared across imaging sessions to assess repeatability in imaging and quantifying the same pores at different times. Figure 5a–e presents montages of the temporal side of the anterior lamina cribrosa in a normal macaque (M057) from five separate imaging sessions that spanned the course of 128 days. Magnified views of the same region of the lamina cribrosa (denoted by the white box in the corresponding montages) are also shown in Figures 5f–j for each session. Montages of the lamina cribrosa acquired in a normal human eye (H055) in four separate imaging sessions (spanning the course of 233 days) are similarly shown in Figure 6. As seen in all the larger montages and the magnified images, the same pores were clearly visible in each imaging session.

Laminar pores were identified in each eye using the montages acquired at different time points. Laminar pore parameters were calculated and compared within and across imaging sessions. Table 2 summarizes the mean values of the standard deviations in pore area, elongation, and NND calculated after analyzing all pores multiple times within a single imaging session (intrasession) or after analyzing the same pores across all imaging sessions (intersession) in macaques and humans. Only pores that could be imaged and quantified at all time points were included in the calculations of intersession variability. Therefore, 42 and 61 anterior laminar pores were included in monkey eyes M036 and M057, respectively, whereas 15, 22, and 35 were included in human eyes H058, H030, and H055, respectively. The mean variabilities in calculating nearly all pore parameters within and across sessions were slightly lower in macaques than in humans. The intrasession variability was typically much smaller than the intersession variability for all parameters (Table 2), indicating a consistent process for analyzing pore geometry. In macaques, the means of the standard deviations in pore area, elongation, and NND were 50 μm^2 (6.1% of a given pore's mean area), 0.13 (6.7% of a given pore's mean elongation), and 1.93 μm (5.2% of a given pore's mean NND), respectively. For humans, the means of the standard deviations in pore area, elongation, and NND across sessions were 113 μm^2 (8.3% of a given pore's mean area),

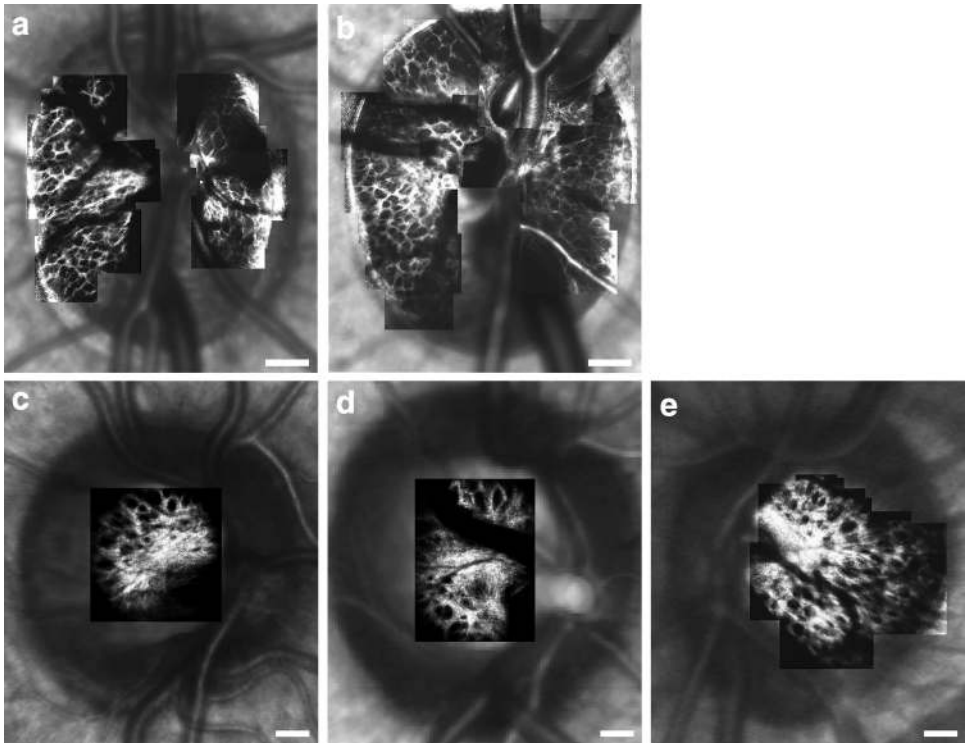

FIGURE 4. AOSLO montages of the anterior lamina cribrosa overlaid on top of SLO images for the (**a**, **b**) macaque and (**c**–**e**) human eyes analyzed in this study. Images show the typical maximum extent over which the lamina was imaged in vivo in each eye. Scale bar, 200 μm.

0.17 (7.7% of a given pore's mean elongation), and 2.79 μm (4.1% of a given pore's mean NND), respectively. There were no statistically significant differences in pore area, elongation, and NND across all imaging sessions in the macaques or the humans (ANOVA, $P > 0.05$), demonstrating good imaging and measurement repeatability.

DISCUSSION

The AOSLO provided high-resolution, high-contrast images of the anterior surface of the lamina cribrosa in normal human and macaque eyes. The values of human laminar pore parameters measured in vivo in this study are comparable to in vivo and ex vivo data from previous reports. Mean laminar pore elongation measured using AOSLO imaging in our three normal human eyes (2.00 ± 0.75) was similar to that measured in vivo by Fontana et al.[26] in 10 normal eyes with a confocal SLO (1.81 ± 0.1). In addition, the range of human pore areas measured in vivo in this study (154–6637 μm^2) is comparable to that found ex vivo by Quigley and Addicks[21] (range in pore diameter from 10–100 μm, or in pore area from ~79–7850 μm^2 assuming circular pores) and by Dandona et al.[36] in nine normal histologic samples sectioned midway between the anterior and posterior laminar surfaces (range of 410 ± 35 to 5201 ± 621 μm^2 for the 10th to 90th percentiles). However, the range of pore areas that we measured in vivo was less than that reported ex vivo by Ogden et al.,[37] (500–22,500 μm^2) and our mean pore area (1713 ± 1414 μm^2) was also less than that measured ex vivo by Jonas et al. [38] (4000 ± 1000 μm^2) at the anterior laminar surface in 35 normal eyes.

Many factors could account for the discrepancies in the range and mean values of pore areas between our in vivo measures in human eyes and the latter two ex vivo reports. Several postmortem studies support the idea that human laminar pores tend to be largest in the superior and inferior poles of the ONH and increase in size toward the periphery of the nerve.[21,37] As mentioned earlier, it was difficult to image laminar pores in vivo at the superior and inferior poles in most eyes as the overlying vasculature (e.g., the central retinal artery and vein) typically obstructs the visualization of these pores. In addition, the neuroretinal rim can cast shadows on to the anterior laminar surface, prohibiting the visualization of the

TABLE 1. Pore Geometry in Normal Macaque and Human Eyes

	Area (μm^2)		Elongation		NND (μm)	
	Mean ± Standard Deviation	Range	Mean ± Standard Deviation	Range	Mean ± Standard Deviation	Range
Normal macaque eyes						
M036	870 ± 610	90–3439	1.90 ± 0.77	1.10–5.28	37.9 ± 7.62	17.8–54.7
M057	1055 ± 907	122–4365	1.66 ± 0.54	1.06–4.79	36.0 ± 6.70	19.6–54.1
All eyes	973 ± 794	90–4365	1.77 ± 0.66	1.06–5.28	36.9 ± 7.19	17.8–54.7
Normal human eyes						
H030	1603 ± 1481	227–5568	1.85 ± 0.60	1.17–3.39	60.9 ± 17.0	29.3–94.5
H055	1769 ± 1296	154–5560	2.14 ± 0.91	1.10–4.83	68.3 ± 16.9	37.1–114
H058	1732 ± 1642	299–6637	1.88 ± 0.43	1.30–2.65	81.5 ± 25.6	52.5–125
All eyes	1713 ± 1414	154–6637	2.00 ± 0.75	1.10–4.83	69.1 ± 19.8	29.3–125

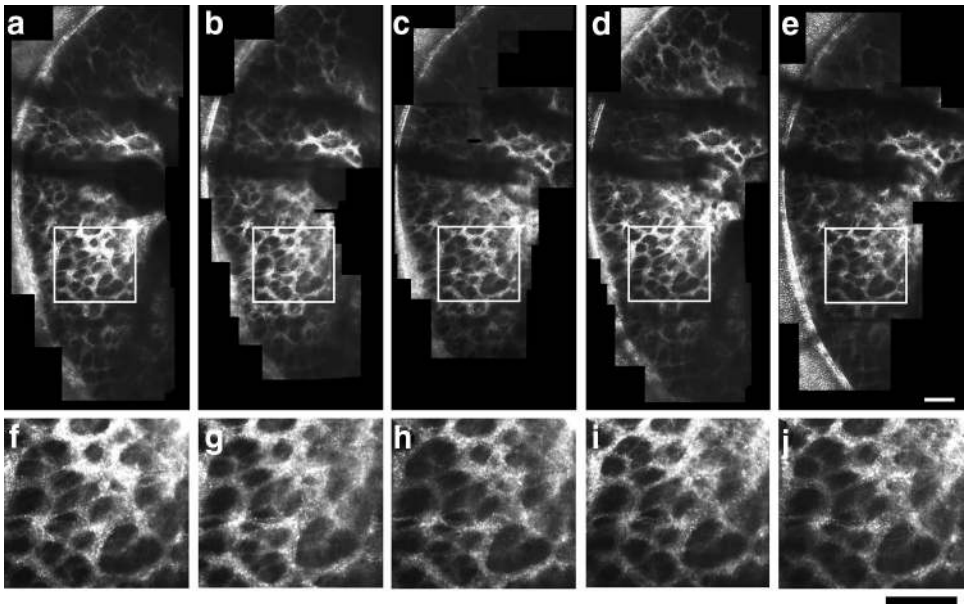

FIGURE 5. (**a–e**) Montages of the temporal side of the anterior lamina cribrosa taken in a normal macaque (M057) over five different imaging sessions (spanning 128 days). Vasculature overlying the laminar surface cast shadows on and obstruct the visualization of the underlying laminar pores. (**f–j**) Magnified images of the same patch of lamina denoted by the white squares in images (**a–e**). The same laminar pores could be imaged consistently across sessions. Scale bar, 100 μm.

most peripheral laminar pores in these circumstances. Therefore, it is possible that we did not image the largest laminar pores in vivo in all our human eyes and that our measures of laminar pore area underestimate some of those found ex vivo.

Another possible confounding factor is that the en face AOSLO images represent a two-dimensional projection of a potentially curved three-dimensional anterior laminar surface. Strouthidis et al.[39] recently demonstrated the ability to subjectively identify a contour representing the anterior laminar surface in a primate eye from a cross-sectional image of the ONH acquired using spectral domain OCT. The position of the anterior laminar surface was not measured in our study eyes. Consequently, our AOSLO pore parameters may not represent the true anatomic shape of laminar pores in eyes with nonplanar anterior laminar surfaces. Although it is unknown the extent to which a three-dimensional transformation will alter our measured pore values, we do expect to see larger differences in eyes with more steeply curved anterior laminar surfaces. Therefore, our measured values could represent a lower bound for the true anatomic sizes imaged in vivo. Knowledge of absolute pore geometry may be important for biomechanical modeling of the anterior laminar surface. However, it may not be necessary for detecting changes in laminar pores during early experimental glaucoma in which one may be interested in detecting a relative change in pore structure in relation to the occurrence of changes in other clinical parameters conventionally used to diagnose and assess glaucoma.

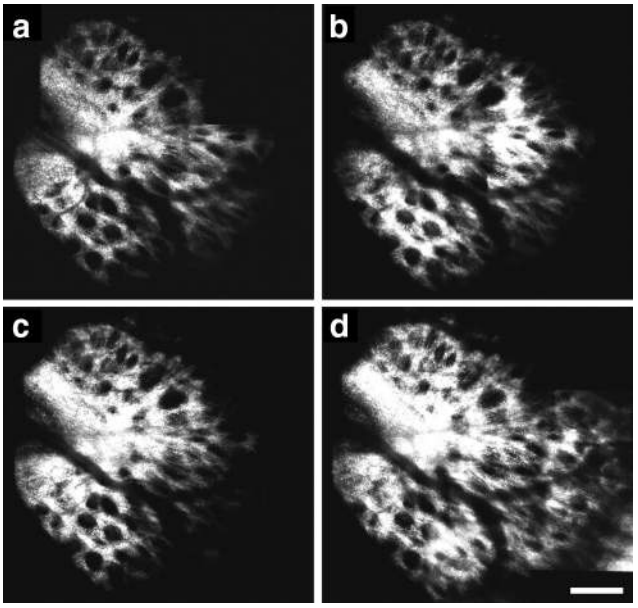

FIGURE 6. (**a–d**) Montages of the anterior lamina cribrosa taken in a normal human eye (H055) over four different imaging sessions (spanning 233 days). The same laminar pore structure could be imaged consistently across sessions. A slightly larger laminar area was imaged in (**d**) due to advances in our imaging methods. Scale bar, 200 μm.

Laminar pore parameters measured in vivo in our two normal nonhuman primate eyes can also be compared with the same values measured by Vilupuru et al.[27] in four living macaque control eyes with a different AOSLO. Whereas both studies yielded comparable values of mean pore elongation in normal, control eyes (1.77 in the present study vs. ~1.6 in Vilupuru et al.), mean pore area and NND were larger in Vilupuru et al. (~1950 μm^2 and ~47 μm, respectively) than in the present study (973 μm^2 and 37 μm, respectively). The reasons for these discrepancies in pore area and NND are not clear. We do not know whether the resolution and confocality (e.g., pinhole diameter) of the AOSLO used in this study differed from that used by Vilupuru et al., potentially allowing us to better visualize and define the boundaries of smaller pores. Another possibility is that a different number of pores were analyzed in each study. In addition, it is possible that these differences simply represent intersubject variability in laminar pore geometry given the small number of macaques imaged in this study ($n = 2$) and by Vilupuru et al. ($n = 4$). Attempts are currently underway to image anterior laminar pore parameters in a greater number of eyes to better define this issue in the normal macaque.

A main goal of this work was to examine the variability in our laminar pore measurements over time. Because we wanted to assess the repeatability with which we could quantify the same laminar pores at each imaging time point, we used a repeated-measures ANOVA to assess the statistical variability in our measurements. A limitation of using a repeated-measures ANOVA is that one can only include pores that were quantified in all imaging sessions. For example, improvements in our

TABLE 2. Variability in Anterior Laminar Pore Geometry Measured in Normal Macaque and Human Eyes within (Intrasession) and across (Intersession) Imaging Sessions

	Standard Deviation of Area (μm^2)		Standard Deviation of Elongation		Standard Deviation of NND (μm)	
	Intrasession	**Intersession**	**Intrasession**	**Intersession**	**Intrasession**	**Intersession**
Macaque	13 (2.2%)	50 (6.1%)	0.04 (1.4%)	0.13 (6.7%)	0.10 (0.2%)	1.93 (5.2%)
Human	22 (0.9%)	113 (8.3%)	0.01 (0.5%)	0.17 (7.7%)	0.31 (0.2%)	2.79 (4.1%)

Data are mean standard deviations (percentage of pore parameter).

imaging and quantification techniques typically enabled us to examine a greater extent of the laminar surface in a given eye over time, thereby allowing us (in general) to quantify a greater number of pores at the end of the experiment. (Fig. 6d represents an example in which we were able to image a greater extent of the laminar surface due to improved techniques.) However, even though an increased number of pores could often be visualized at later time points, these additional pores were not included in the repeated-measures ANOVA for a given eye if they were not imaged at all earlier time points. In addition, although it was possible to measure and track the same laminar pores at multiple time points, we excluded pores from the ANOVA even if they were quantified in all but one session. As a result, the number of pores that were quantified and used to assess repeatability across all imaging sessions was less than the total number of pores used to generate the global statistics on mean pore area, elongation, and NND in a given eye.

This study's method for imaging and quantifying anterior laminar pores with an AOSLO is repeatable in normal eyes. No statistically significant differences were found in pore geometry (ANOVA, $P > 0.05$) when comparing laminar pore parameters measured in the same eyes imaged over multiple time points. Intrasession variability was also small (Table 2), demonstrating a consistent means for identifying pores. Mean pore area tended to have the largest measured intersession variability (Table 2, mean standard deviation of 8.3% in humans and 6.1% in macaques). This variability was likely due to small intensity differences between the AOSLO reflectance images acquired across imaging sessions (potentially caused by slight differences in illumination levels, retinal reflectivity, or photomultiplier detector gain). For example, making only a half-pixel error in the identification of the entire boundary of the pores analyzed in this study would result in a 5.1% and 4.5% difference in mean pore area (on average) in humans and macaques, respectively. These values are not vastly dissimilar from our measured variabilities in mean pore area. Also, despite demonstrating good repeatability, the subjective methods used for demarcating and quantifying laminar pores can be very time-consuming and could be challenging to apply to the analysis of several eyes over short periods. We are currently developing algorithms to make this pore analysis method more objective and to decrease the required processing time through the use of semiautomated image processing techniques.

Even though it is possible to acquire excellent en face images of the anterior laminar surface in living eyes, AOSLO imaging is limited in its ability to visualize the entire laminar structure in three dimensions. Therefore, it may not be possible to use this technique to examine changes throughout the entire extent of the lamina in glaucoma. Nevertheless, it is still possible to visualize laminar pores over a finite range in depth behind the anterior laminar surface (Fig. 1) despite the AOSLO's limited axial resolution.[40] In addition, current models propose that changes in laminar thickness and position occur throughout the entire thickness of the lamina in early experimental glaucoma.[41] Therefore, changes in laminar pores should also occur at all depths, including the anterior surface which is visible using AOSLO imaging.

In conclusion, we have established a repeatable method for relocating the same laminar pores and quantifying their geometries in vivo in normal human and nonhuman primate eyes. The methods presented in this article could be extended to assess longitudinal changes in laminar pore structure in glaucomatous neuropathy. These measurements would contribute to a broader and more detailed understanding of the biomechanical properties of the normal and glaucomatous lamina while also enabling the correlation of laminar pore changes with functional and structural changes conventionally used to diagnose glaucoma.

Acknowledgments

The authors thank Harold Bedell, Claude Burgoyne, Crawford Downs, Laura Frishman, and Michael Twa for helpful discussions.

References

1. Anderson DR, Hendrickson A. Effect of intraocular pressure on rapid axoplasmic transport in monkey optic nerve. *Invest Ophthalmol.* 1974;13:771–783.
2. Anderson DR, Hendrickson AE. Failure of increased intracranial pressure to affect rapid axonal transport at the optic nerve head. *Invest Ophthalmol Vis Sci.* 1977;16:423–426.
3. Howell GR, Libby RT, Jakobs TC, et al. Axons of retinal ganglion cells are insulted in the optic nerve early in DBA/2J glaucoma. *J Cell Biol.* 2007;179:1523–1537.
4. Minckler DS, Spaeth GL. Optic nerve damage in glaucoma. *Surv Ophthalmol.* 1981;26:128–148.
5. Quigley H, Anderson DR. The dynamics and location of axonal transport blockade by acute intraocular pressure elevation in primate optic nerve. *Invest Ophthalmol.* 1976;15:606–616.
6. Quigley HA, Addicks EM. Chronic experimental glaucoma in primates. II. Effect of extended intraocular pressure elevation on optic nerve head and axonal transport. *Invest Ophthalmol Vis Sci.* 1980;19:137–152.
7. Quigley HA, Addicks EM, Green WR, Maumenee AE. Optic nerve damage in human glaucoma. II. The site of injury and susceptibility to damage. *Arch Ophthalmol.* 1981;99:635–649.
8. Quigley HA, Anderson DR. Distribution of axonal transport blockade by acute intraocular pressure elevation in the primate optic nerve head. *Invest Ophthalmol Vis Sci.* 1977;16:640–644.
9. Quigley HA, Flower RW, Addicks EM, McLeod DS. The mechanism of optic nerve damage in experimental acute intraocular pressure elevation. *Invest Ophthalmol Vis Sci.* 1980;19:505–517.
10. Quigley HA, Guy J, Anderson DR. Blockade of rapid axonal transport: effect of intraocular pressure elevation in primate optic nerve. *Arch Ophthalmol.* 1979;97:525–531.
11. Quigley HA, Hohman RM, Addicks EM, Massof RW, Green WR. Morphologic changes in the lamina cribrosa correlated with neural loss in open-angle glaucoma. *Am J Ophthalmol.* 1983;95:673–691.
12. Downs JC, Roberts MD, Burgoyne CF. Mechanical environment of the optic nerve head in glaucoma. *Optom Vis Sci.* 2008;85:425–435.

13. Bellezza AJ, Hart RT, Burgoyne CF. The optic nerve head as a biomechanical structure: initial finite element modeling. *Invest Ophthalmol Vis Sci.* 2000;41:2991–3000.
14. Sigal IA, Flanagan JG, Tertinegg I, Ethier CR. Finite element modeling of optic nerve head biomechanics. *Invest Ophthalmol Vis Sci.* 2004;45:4378–4387.
15. Roberts MD, Liang Y, Sigal IA, et al. Correlation between local stress and strain and lamina cribrosa connective tissue volume fraction in normal monkey eyes. *Invest Ophthalmol Vis Sci.* 2010;51:295–307.
16. Bellezza AJ, Rintalan CJ, Thompson HW, Downs JC, Hart RT, Burgoyne CF. Deformation of the lamina cribrosa and anterior scleral canal wall in early experimental glaucoma. *Invest Ophthalmol Vis Sci.* 2003;44:623–637.
17. Anderson DR. Ultrastructure of human and monkey lamina cribrosa and optic nerve head. *Arch Ophthalmol.* 1969;82:800–814.
18. Hernandez MR. The optic nerve head in glaucoma: role of astrocytes in tissue remodeling. *Prog Retin Eye Res.* 2000;19:297–321.
19. Yang H, Downs JC, Bellezza A, Thompson H, Burgoyne CF. 3-D histomorphometry of the normal and early glaucomatous monkey optic nerve head: prelaminar neural tissues and cupping. *Invest Ophthalmol Vis Sci.* 2007;48:5068–5084.
20. Roberts MD, Grau V, Grimm J, et al. Remodeling of the connective tissue microarchitecture of the lamina cribrosa in early experimental glaucoma. *Invest Ophthalmol Vis Sci.* 2009;50:681–690.
21. Quigley HA, Addicks EM. Regional differences in the structure of the lamina cribrosa and their relation to glaucomatous optic nerve damage. *Arch Ophthalmol.* 1981;99:137–143.
22. Emery JM, Landis D, Paton D, Boniuk M, Craig JM. The lamina cribrosa in normal and glaucomatous human eyes. *Trans Am Acad Ophthalmol Otolaryngol.* 1974;78:OP290–OP297.
23. Hernandez MR, Andrzejewska WM, Neufeld AH. Changes in the extracellular-matrix of the human optic-nerve head in primary open-angle glaucoma. *Am J Ophthalmol.* 1990;109:180–188.
24. Walsh MK, Quigley HA. In vivo time-lapse fluorescence imaging of individual retinal ganglion cells in mice. *J Neurosci Methods.* 2008;169:214–221.
25. Yang H, Thompson H, Roberts MD, Sigal IA, Downs JC, Burgoyne CF. Deformation of the early glaucomatous monkey optic nerve head connective tissue following acute IOP elevation within 3-D histomorphometric reconstructions. *Invest Ophthalmol Vis Sci.* 2010;52:345–363.
26. Fontana L, Bhandari A, Fitzke FW, Hitchings RA. In vivo morphometry of the lamina cribrosa and its relation to visual field loss in glaucoma. *Curr Eye Res.* 1998;17:363–369.
27. Vilupuru AS, Rangaswamy NV, Frishman LJ, Smith EL 3rd, Harwerth RS, Roorda A. Adaptive optics scanning laser ophthalmoscopy for in vivo imaging of lamina cribrosa. *J Opt Soc Am A Opt Image Sci Vis.* 2007;24:1417–1425.
28. Torti C, Povazay B, Hofer B, et al. Adaptive optics optical coherence tomography at 120,000 depth scans/s for non-invasive cellular phenotyping of the living human retina. *Opt Express.* 2009;17:19382–19400.
29. Zawadzki RJ, Choi SS, Fuller AR, Evans JW, Hamann B, Werner JS. Cellular resolution volumetric in vivo retinal imaging with adaptive optics-optical coherence tomography. *Opt Express.* 2009;17:4084–4094.
30. Frishman LJ, Shen FF, Du L, et al. The scotopic electroretinogram of macaque after retinal ganglion cell loss from experimental glaucoma. *Invest Ophthalmol Vis Sci.* 1996;37:125–141.
31. Qiao-Grider Y, Hung LF, Kee CS, Ramamirtham R, Smith EL, 3rd. A comparison of refractive development between two subspecies of infant rhesus monkeys (Macaca mulatta). *Vision Res.* 2007;47:1668–1681.
32. Li KY, Tiruveedhula P, Roorda A. Intersubject variability of foveal cone photoreceptor density in relation to eye length. *Invest Ophthalmol Vis Sci.* 2010;51:6858–6867.
33. ANSI. *American National Standard for Safe Use of Lasers.* Orlando, FL: The Laser Institute of America; 2007:ANSI 136.1-2007.
34. Delori FC, Webb RH, Sliney DH. Maximum permissible exposures for ocular safety (ANSI 2000), with emphasis on ophthalmic devices. *J Opt Soc Am A Opt Image Sci Vis.* 2007;24:1250–1265.
35. Li C, Sredar N, Ivers KM, Queener H, Porter J. A correction algorithm to simultaneously control dual deformable mirrors in a woofer-tweeter adaptive optics system. *Opt Express.* 2010;18:16671–16684.
36. Dandona L, Quigley HA, Brown AE, Enger C. Quantitative regional structure of the normal human lamina cribrosa: a racial comparison. *Arch Ophthalmol.* 1990;108:393–398.
37. Ogden TE, Duggan J, Danley K, Wilcox M, Minckler DS. Morphometry of nerve fiber bundle pores in the optic nerve head of the human. *Exp Eye Res.* 1988;46:559–568.
38. Jonas JB, Mardin CY, Schlotzer-Schrehardt U, Naumann GO. Morphometry of the human lamina cribrosa surface. *Invest Ophthalmol Vis Sci.* 1991;32:401–405.
39. Strouthidis NG, Grimm J, Williams GA, Cull GA, Wilson DJ, Burgoyne CF. A comparison of optic nerve head morphology viewed by spectral domain optical coherence tomography and by serial histology. *Invest Ophthalmol Vis Sci.* 2010;51:1464–1474.
40. Romero-Borja F, Venkateswaran K, Roorda A, Hebert T. Optical slicing of human retinal tissue in vivo with the adaptive optics scanning laser ophthalmoscope. *Appl Opt.* 2005;44:4032–4040.
41. Burgoyne CF, Downs JC. Premise and prediction-how optic nerve head biomechanics underlies the susceptibility and clinical behavior of the aged optic nerve head. *J Glaucoma.* 2008;17:318–328.